Lawrence Berkeley National Laboratory
LBL Publications

Title
Filament Formation in TaOx Thin Films for Memristor Device Application: Modeling Electron Energy Loss Spectra and Electron Transport

Permalink
https://escholarship.org/uc/item/8x13d8x8

Journal
Advanced Electronic Materials, 9(1)

ISSN
2199-160X

Authors
Jiang, Jie
Pachter, Ruth
Mahalingam, Krishnamurthy
et al.

Publication Date
2023

DOI
10.1002/aelm.202200828

Copyright Information
This work is made available under the terms of a Creative Commons Attribution License, available at https://creativecommons.org/licenses/by/4.0/

Peer reviewed

eScholarship.org Powered by the California Digital Library
University of California

Optimizing Interface Conductivity in Electronics

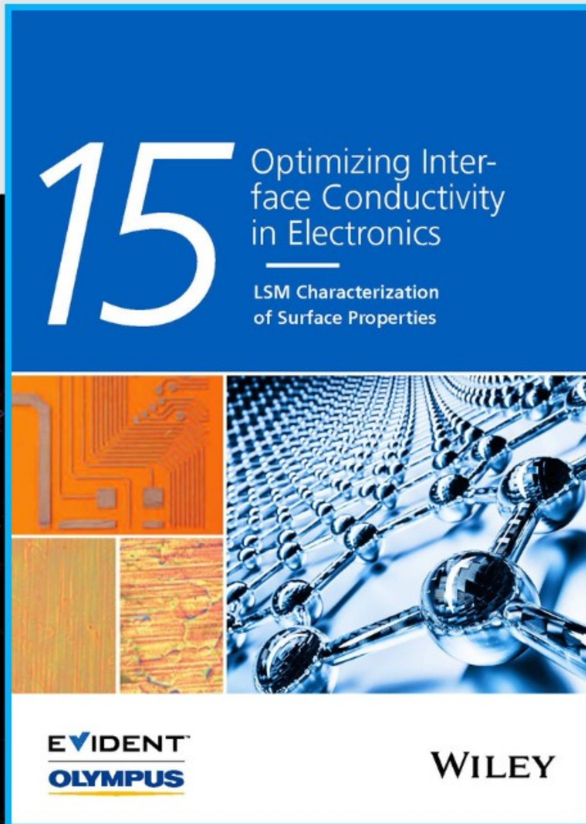

The latest eBook from Advanced Optical Metrology. Download for free.

Surface roughness is a key parameter for judging the performance of a given material's surface quality for its electronic application. A powerful tool to measure surface roughness is 3D laser scanning confocal microscopy (LSM), which will allow you to assess roughness and compare production and finishing methods, and improve these methods based on mathematical models.

Focus on creating high-conductivity electronic devices with minimal power loss using laser scanning microscopy is an effective tool to discern a variety of roughness parameters.

EVIDENT

OLYMPUS

WILEY

Check for updates

ADVANCED ELECTRONIC MATERIALS
www.advelectronicmat.de

Filament Formation in TaO_x Thin Films for Memristor Device Application: Modeling Electron Energy Loss Spectra and Electron Transport

Jie Jiang, Ruth Pachter, Krishnamurthy Mahalingam, Jim Ciston, Rohan Dhall, Robert J. Bondi, Matthew J. Marinella, Donald A. Telesca, and Sabyasachi Ganguli*

Although understanding filament formation in oxide-based memristive devices by theory has emerged, there are still fundamental unanswered questions. Importantly, for practical application of thin films the material in its amorphous state is to be considered, but mostly lacking so far, and details on sub-stoichiometry are also scarce. To gain insight into the optical and electronic properties of sub-stoichiometric amorphous tantalum oxide (TaO_x), the electron energy loss spectrum (EELS) of model systems is characterized theoretically and electron transport characteristics are analyzed in detail. Calculated blue-shifts by increasing sub-stoichiometry explained the measurements, potentially suggesting estimation of oxygen vacancy concentrations through EEL spectra. Electron transport results based on TaO_x material models validated by EELS measurements show that oxygen vacancy filamentary paths are initiated at low bias upon increasing sub-stoichiometry yet noting an interplay with the local amorphous structure. Contact resistances at interfaces of the TaO_x switching layer and a tantalum scavenging layer or titanium nitride electrode are quantified, indicating the possibility for either oxygen vacancy- or metal cluster-based conduction mechanisms at the interface. The computational work, combined with experimental characterization for validation, provides a basis for investigating effects of sub-stoichiometry on filament formation in TaO_x thin film memristive devices.

1. Introduction

Resistive random access memory (ReRAM) devices have drawn much interest following the work of Williams and co-workers,[1] as based on the concept of a memristor proposed by Chua.[2] In this case the so-called memristance, which provides the relationship between the change in charge (time integral of the current) and flux (time integral of the voltage), is not a constant as in linear elements, but a function of the charge, resulting in a nonlinear circuit element. Focus on filamentary-type resistive switching mechanisms emerged, where formation/rupture of a conductive filament ensures successive switching in non-volatile metal-insulator-metal memristor devices. In such devices, metal oxide structures are stacked between two electrodes, which can be either symmetric or asymmetric by using the same or different top and bottom electrodes, respectively. In the filamentary resistive switching mechanism between a high-resistance state (HRS) and

J. Jiang, R. Pachter, K. Mahalingam, S. Ganguli
Air Force Research Laboratory
Materials and Manufacturing Directorate
Wright-Patterson Air Force Base, Dayton, OH 45433, USA
E-mail: ruth.pachter@us.af.mil

J. Ciston, R. Dhall
National Center for Electron Microscopy
Molecular Foundry
Lawrence Berkeley National Laboratory
Berkeley, CA 94720, USA

The ORCID identification number(s) for the author(s) of this article can be found under https://doi.org/10.1002/aelm.202200828.

© 2022 The Authors. Advanced Electronic Materials published by Wiley-VCH GmbH. This is an open access article under the terms of the Creative Commons Attribution License, which permits use, distribution and reproduction in any medium, provided the original work is properly cited.

DOI: 10.1002/aelm.202200828

R. J. Bondi
Quantum Generative Materials LLC
Cheyenne, WY 82001, USA

M. J. Marinella
School of Electrical
Computer and Energy Engineering
Arizona State University
Tempe, AZ 85281, USA

D. A. Telesca
Air Force Research Laboratory
Information Directorate
Rome, NY 13441, USA

a low-resistance state (LRS) following the conducting filament forming stage, where a compliance current is used for controlling its size, operation depends on the migration of ions across the metal oxide in the so-called SET (RESET) stages upon application of positive (negative) voltage in a bipolar ReRAM, or the same polarity voltage in a unipolar system. The rupture of the conducting filament causes a HRS and its re-formation results in a LRS. The devices provide high integration densities and low-power operation and can find utility for instance, as neuromorphic-type computing elements.

This area of research led to numerous reviews[3–6] (see citing and cited references). Indeed, memristive devices offer advantages in enabling increased speed of operation, higher density, non-volatility, ease of integration, and low power. The underlying mechanism of operation varies, depending on the oxide layer and the electrodes, where oxygen vacancies play an important role.[7,8] In valence change memory cells, resistive switching is attributed to the formation and rupture of oxygen vacancy (V_O)-based conductive filaments. However, although a basic understanding of the resistive switching in this case was established to some extent, as reviewed by Yang and co-workers,[9] specific details are still a topic of debate. Better understanding of the mechanism will enable realizing more fully the potential of a ReRAM as a highly scalable, commercially viable device.

Among the metal oxides, sub-stoichiometric tantalum oxide (TaO_x) emerged as a promising candidate[10,11] for ReRAM applications because of its endurance,[12] speed of operation,[13] and in providing multiple resistance levels due to triple switching regimes,[14] therefore selected for this study. The high endurance of TaO_x-based ReRAM devices was attributed to a stable amorphous phase and adaptive lattice rearrangements of its oxygen vacancies.[15] Note that it was recently demonstrated by synchrotron-based X-ray photoemission electron microscopy that there is no indication of a metallic Ta filament in TaO_x memristive devices.[16] In addition, adding an interfacial layer is assumed to provide a reservoir of oxygen defects and improve the reliability of resistive switching devices.[17]

Theoretically, to explain the mechanism of resistive switching and suggest potential improvements in addressing the encountered challenges, first-principles computational studies were reported, for instance for Ta_2O_5,[18] TiO_2,[19] HfO_2,[20] and NiO,[21] assuming crystalline structures in all cases. The effect of introducing dopants to tune oxygen vacancy formation in transition metal oxide resistive memory materials was also investigated by first-principles calculations for crystalline and amorphous Ta_2O_5 model systems,[22] as well as for crystalline structures, for example, ZrO_2.[23] Indeed, to provide reasonable understanding of the switching phenomenon by atomic-level calculations, a realistic representation of the oxide in its amorphous state is necessary. Previously we investigated the effects of oxygen vacancies in amorphous material models of Ta_2O_5,[24–27] and this approach was also utilized to examine the phase separation of Ta_2O_5 and TaO_2,[28] however without consideration of filament formation characteristics. Moreover, although phenomenological modeling of memristive devices has been employed,[29] such as in considering the electric field and oxygen vacancy concentration in a TaO_x-based device[30] or in modeling thermodiffusion,[16] establishing the atomic-level characteristics for amorphous thin films that influence the parameters in the models used is lacking. As was previously noted, the applied phenomenological equations represent only an educated guess and different behavior can be observed upon changing the device setting.[31]

In this study, we address several questions on filament formation in amorphous TaO_x at the atomic level. To validate the model systems employed, we characterized the electron energy loss spectrum (EELS) of the materials theoretically (the structures considered are shown in Figure S1, Supporting Information) in comparison to our experimental EELS measurements. We employed a rigorous approach, where many-body calculations were benchmarked in comparison to a density functional theory (DFT)-based method. EELS measurements for TaO_x were previously reported,[32,33] however in the latter case the measurements were conducted for a ReRAM device that operated inside a transmission electron microscopy (TEM) system. As our goal was to study the intrinsic behavior of the material, we compare our results to ref. [32] as well. Encouragingly, we demonstrated consistency with experimental data considering the simplified material models, and moreover we rationalized the calculated and experimentally observed blue-shift upon increase of sub-stoichiometry. We investigated filament formation for sub-stoichiometric amorphous structures by electron transport calculations, as based on the experimental validation, in part, of the material models by EELS. The intrinsic electron transmission results are explained in detail by the formation of transmission paths, where sub-stoichiometric TaO_x demonstrated generation of oxygen vacancy filaments at low bias voltage. Effects of the interface with a tantalum (Ta) scavenging layer or directly with a titanium nitride (TiN) electrode were studied by deriving appropriate interface model systems for crystalline and amorphous TaO_x including detailed analyses of the conduction mechanisms at the TaO_x/Ta and TaO_x/TiN interfaces.

2. Results and Discussion

Our EELS measurements were performed on bulk Ta, TaO_x, and the TaO_x/Ta interface (the device structure and material regions corresponding to the EELS profiles are summarized in Figure S2a–c, Supporting Information, and the low-loss regions from the individual layers in Figure S2d, Supporting Information). The EELS data was extracted from the sub-stoichiometric films rather than the TiN/Ta/TaO_x/TiN device, whose resistive switching was previously reported.[34] The distinct difference in the measured profiles extracted from the TaO_x and Ta regions are in agreement with those reported in an earlier study using reflection EELS.[32] Calculated spectra are shown in **Figure 1**a,b, including our EELS profile measurements and the results from ref. [32]. EEL spectra were first calculated for crystalline *c*Ta and *c*Ta_2O_5, where small unit cell sizes enabled employing the many-body G_0W_0 (GW henceforth) method (G-Green's function, which describes the particle in an interacting system and W-screened Coulomb interaction; computational details are summarized in the Experimental Section) in comparison to corresponding amorphous systems and experimental data. Note that a typical feature for the valence-loss spectrum is a broad peak at the plasma energy $E_p = \hbar\sqrt{\frac{ne^2}{\varepsilon_0 m_e}}$ (ħ, n, e, ε_0, and m_e are the reduced Planck

© 2022 The Authors. Advanced Electronic Materials published by Wiley-VCH GmbH

2199160x, 2023, 1, Downloaded from https://onlinelibrary.wiley.com/doi/10.1002/aelm.202200828, Wiley Online Library on [26/07/2023]. See the Terms and Conditions (https://onlinelibrary.wiley.com/terms-and-conditions) on Wiley Online Library for rules of use; OA articles are governed by the applicable Creative Commons License

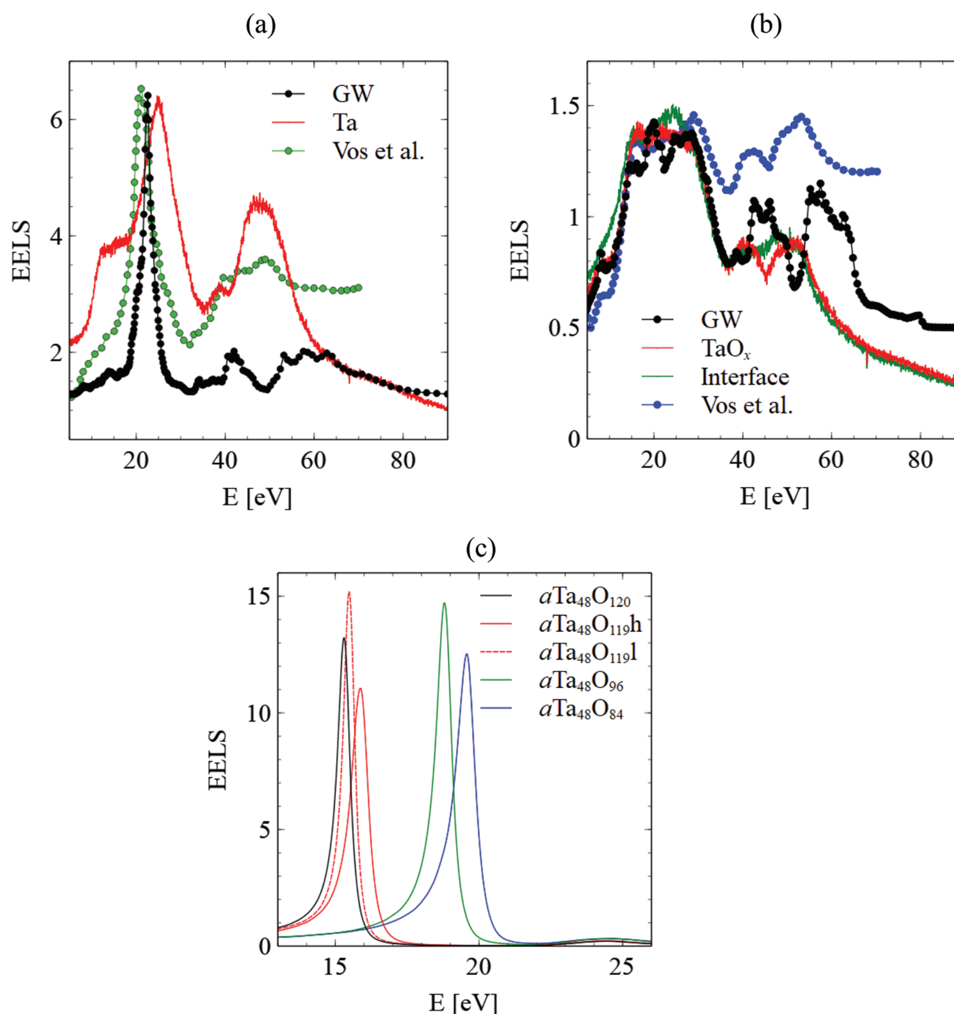

Figure 1. GW EEL spectra (black line) for a) cTa and b) cTa$_2$O$_5$. a) Our and ref. [32] EELS measurements on Ta are shown in red and green lines, respectively. b) Our measurements on Ta$_2$O$_x$ and the Ta$_2$O$_x$/Ta interface, and from ref. [32] for Ta$_2$O$_5$, are shown in red, green, and blue, respectively. c) HSE EELS results for aTa$_{48}$O$_x$ with varying sub-stoichiometry.

constant, valence electron density, electron charge, permittivity of vacuum, and the effective mass of the electron, respectively, indicating proportionality to the density of the valence electrons and inverse proportionality to the electron effective mass) that is repeated with decreased intensity at $2E_p$, $3E_p$, etc.

In **Table 1**, we list the peak positions, full width at half maximum, and peak intensities relative to the first peak, with three major peaks in addition to a shoulder in the low-energy region (typically <50 eV) of the EEL spectra. Our GW calculations demonstrate that there are three visible peaks at approximately E_p, $2E_p$, and $3E_p$ for the cTa and cTa$_2$O$_5$ spectra, in agreement with our measurements. In examining the peaks in the EEL spectra for cTa, we find that the predicted first and second EELS peaks agree well with measurements, but the third peak is higher in energy. The full width at half maximum (FWHM) is smaller than the measured value for the first peak, and the relative intensities are weaker than our measurements. For the four peaks of cTa$_2$O$_5$, we note a weak peak at low energy (7.9 eV), as also observed in our measurement and by Vos et al.[32] The calculated and measured strong peaks are consistent in energy and intensity. The first strong peak at 22.3 eV is broad, with a FWHM value of ≈20 eV, consisting of three sub-peaks in agreement with measurements in energy, FWHM, and line shape. The second peak at 44.9 eV agrees with measurements in position and FWHM, while the calculated third peak demonstrated higher energy than the measured data but the FWHM is close to our measurement and ref. [32]. The predicted relative intensities are larger than our characterization values, but smaller than previously measured,[32] depending on the experimental samples considered. The GW EELS results for cTa and cTa$_2$O$_5$ agree with our measurements reasonably well, correctly predicting the number of peaks in the experimental energy region, in particular the peak energies for the shoulder and first two peaks. Discrepancies are attributed to the crystalline rather than amorphous Ta and Ta$_2$O$_5$ atomic structures employed. However, our GW results provide a theoretical benchmark in comparing to DFT results employing the Heyd-Scuseria-Ernzerhof (HSE) hybrid range-separated exchange correlation functional.

Calculations of EEL spectra at the GW level for amorphous Ta$_{48}$O$_{120-x}$ (≈160 atoms) are not feasible computationally and we therefore benchmarked calculations that employ the random

 © 2022 The Authors. Advanced Electronic Materials published by Wiley-VCH GmbH

2199160x, 2023, 1, Downloaded from https://onlinelibrary.wiley.com/doi/10.1002/aelm.202200828, Wiley Online Library on [26/07/2023]. See the Terms and Conditions (https://onlinelibrary.wiley.com/terms-and-conditions) on Wiley Online Library for rules of use; OA articles are governed by the applicable Creative Commons License

2199160x, 2023, 1, Downloaded from https://onlinelibrary.wiley.com/doi/10.1002/aelm.202200828, Wiley Online Library on [26/07/2023]. See the Terms and Conditions (https://onlinelibrary.wiley.com/terms-and-conditions) on Wiley Online Library for rules of use; OA articles are governed by the applicable Creative Commons License

Table 1. Peak positions (in eV), FWHM values (in eV), and relative intensity to the first peak (I) for *c*Ta and *c*Ta_2O_5.

*c*Ta		Peak 1		Peak 2			Peak 3		
	E	*E*	FWHM	*E*	FWHM	*I*	*E*	FWHM	*I*
Theory	14.1	22.6	2.7	41.5	4.4	0.31	58.5	14.1	0.31
This work (exp.)	15.3	24.8	5.8	38.6	2.5	0.51	48.1	9.2	0.73
Ref. [32] (exp.)	13.2	21.2	6.3	41.2	5.8	0.50	49.0	7.2	0.55
cTa_2O_5		Peak 1		Peak 2			Peak 3		
	E	*E*	FWHM	*E*	FWHM	*I*	*E*	FWHM	*I*
Theory	7.9	22.3	20.3	44.9	5.2	0.74	59.5	10.2	0.81
This work (exp.) TaO_x	7.9	22.3	20.3	41.0	4.8	0.64	50.9	7.4	0.65
This work (exp.) TaO_x/interface	8.6	22.3	21.5	40.0	4.4	0.61	48.1	7.5	0.68
Ref. [32] (exp.)	7.9	23.3	22.3	42.5	5.4	0.9	53.2	9.1	1.06

phase approximation using HSE for *c*Ta and *c*Ta_2O_5 (Figure S3, Supporting Information, and discussion in Supporting Information). Similar energies were calculated for the first peak by using HSE or GW, thus showing that the HSE results predict E_p reasonably well, and this primary EELS peak at ≈20 eV was used for studying *a*$Ta_{48}O_{120-x}$. The results for *a*$Ta_{48}O_x$ with varying sub-stoichiometry (Figure 1c and Figure S3, Supporting Information) suggest that the structural phase affects primarily details of the EEL line shape, but the peak positions result primarily from the stoichiometry.

With increase of the sub-stoichiometry in amorphous TaO_x we observe a blue-shift in the calculations, where the first lower energy dominant peaks of the EEL spectra for *a*$Ta_{48}O_{120-x}$ were at 15.3, 15.9, 15.5, 18.8, and 19.6 eV for *a*$Ta_{48}O_{120}$, *a*$Ta_{48}O_{119}$h, *a*$Ta_{48}O_{119}$l, *a*$Ta_{48}O_{96}$, and *a*$Ta_{48}O_{84}$, respectively (see Figure 1). The blue-shift is consistent with previous experimental characterization, where the first EELS peak shifted to higher energy with V_O increase.[33] To explain this behavior, we considered as examples *a*$Ta_{48}O_{120}$ and *a*$Ta_{48}O_{84}$ with 0% and 30% V_O, respectively. The real and imaginary parts of the dielectric function are shown in Figure S4a, Supporting Information (black lines for *a*$Ta_{48}O_{120}$ and blue lines for *a*$Ta_{48}O_{84}$), having corresponding E_p values of 15.3 and 19.6 eV that reproduce the EELS peak energies (Equation (6) in the Experimental Section). The valence electron plasma energies are shown by solid arrows in Figure S4a, Supporting Information, indicating that the real part is zero and the imaginary part is small. With the introduction of V_O in *a*$Ta_{48}O_{120}$, the number of valence electrons n (total number of valence electrons in the supercell divided by the supercell volume) decreases, noting that the supercell volume will also decrease when optimized with large sub-stoichiometry. The electron density decreases for 20% and 30% V_O in TaO_x (Figure S4b, Supporting Information), accompanied by an increase in E_p, but increases for a single V_O, which could be attributed to a structural change. As increasing the sub-stoichiometry will decrease the energy gap and increase the metallic character that tends to decrease m_e, the net effect leads to an increase of E_p. This observation could possibly provide a tool to characterize the V_O density in amorphous TaO_x. We also note that the effect on the peak energy for varying amorphous structures with the same Vo concentration, specifically *a*$Ta_{48}O_{119}$h versus *a*$Ta_{48}O_{119}$l, is weaker compared to vacancy concentration effects. For example, the peak energy difference between *a*$Ta_{48}O_{119}$h and *a*$Ta_{48}O_{119}$l is 0.4 eV, while the energy difference between $aT_{48}O_{49}$ and $aT_{48}O_{119}$l is 3.3 eV. The *a*$Ta_{48}O_{120}$, *a*$Ta_{48}O_{119}$h, *a*$Ta_{48}O_{119}$l, *a*$Ta_{48}O_{96}$, and *a*$Ta_{48}O_{84}$ material systems have TaO_x, x values of 2.5, 2.48, 2.48, 2.0, and 1.75, with energy shifts relative to *a*$Ta_{48}O_{120}$ of 0, 0.19, 0.58, 3.51, and 4.28 eV, respectively. The shift increased to 3.51 eV for x of 2–2.5, and to 4.28 eV for x of 1.75, thus making it practical in characterization of x.

Next, we discuss the electron transport characteristics in *a*$Ta_{48}O_{120-x}$, and in the first stage the intrinsic electron transport, where the effect of the electrodes is not considered, corresponding to the transport in the bulk material. To understand variations in the amorphous structure that lead to varying transport characteristics for a given V_O concentration we considered *a*$Ta_{48}O_{119}$l, *a*$Ta_{48}O_{119}$m, and *a*$Ta_{48}O_{119}$h, having a single V_O. We generated 140 structural models by sampling 14 quantum molecular dynamics (MD) configuration snapshots from ten independently quenched structures of *a*$Ta_{48}O_{119}$, where each structure contains a single oxygen vacancy.[24] From this population of structures, we selected three independently quenched structures to exemplify the low-, high-, and mid-level of conductivity. The sub-distributions of conductivity from these three structures cover the entire range of conductivity in the population with minimal overlap. Specific snapshots from each of the three structures were selected as representative configurations: (low) *a*$Ta_{48}O_{119}$l, (medium) *a*$Ta_{48}O_{119}$m, and (high) *a*$Ta_{48}O_{119}$h. The transmission results are shown in **Figure 2**a–c. A unit cell was used for the electrode and a $1 \times 1 \times 2$ supercell was used for the transport channel, which includes two-unit cells along the *z*-axis. For *a*$Ta_{48}O_{119}$l (see Figure S5, Supporting Information) and *a*$Ta_{48}O_{119}$m, the transmission channels at 1.44 and 0.45 eV below the conduction band channels resulted in transmission values of 0.43 and 0.80, respectively, while for *a*$Ta_{48}O_{119}$h there is no transmission channel in the energy gap, indicating the extended nature of the oxygen vacancy and the system is metallic.

The calculated conductance values at zero gate voltage (300 K electron temperature) for *a*$Ta_{48}O_{119}$l, *a*$Ta_{48}O_{119}$m, and *a*$Ta_{48}O_{119}$h, were 1.22×10^{-16}, 3.02×10^{-9}, and 7.49×10^{-6} S,

© 2022 The Authors. Advanced Electronic Materials published by Wiley-VCH GmbH

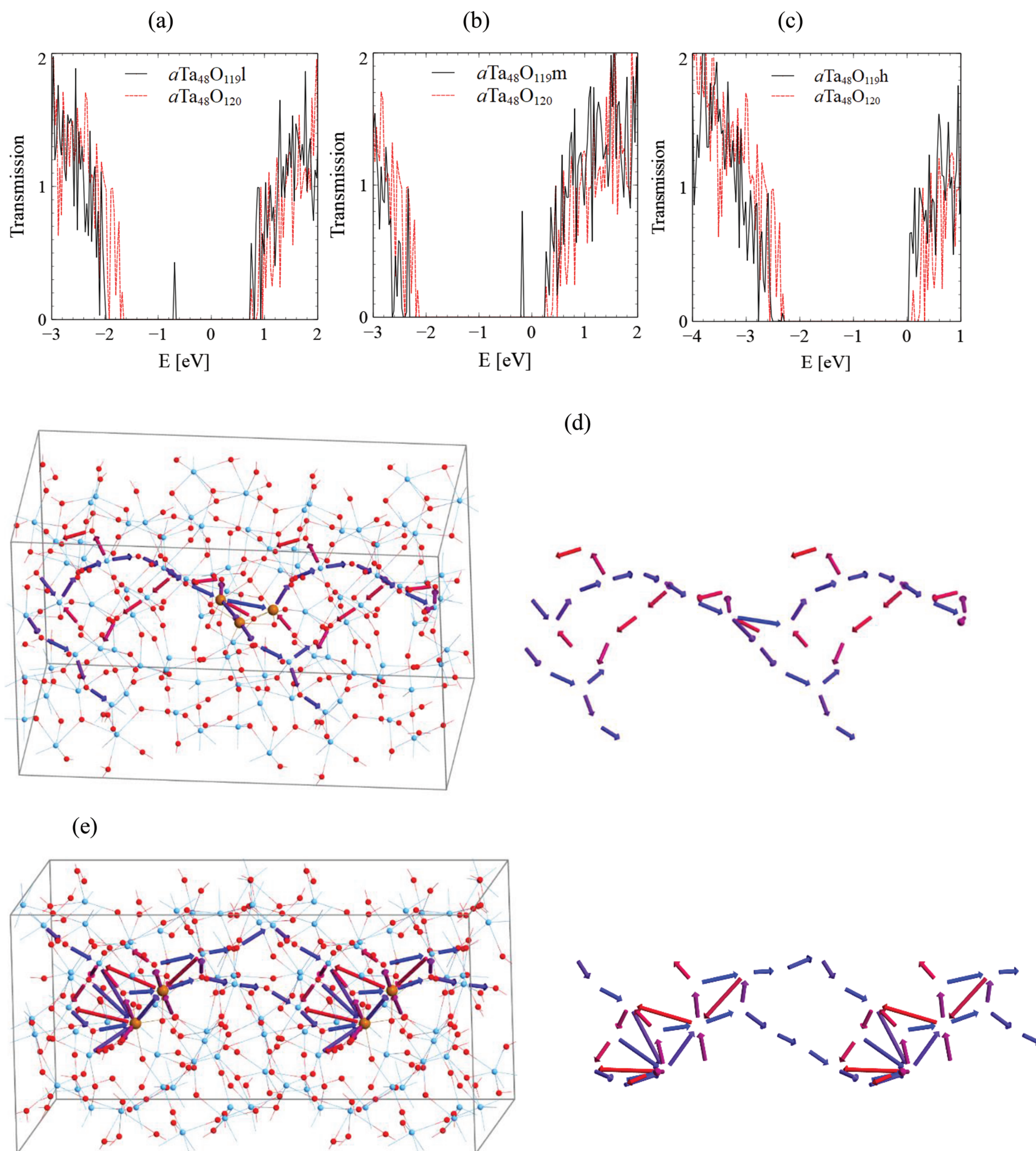

Figure 2. Transmission at zero bias for a) $a\text{Ta}_{48}\text{O}_{119}$l, b) $a\text{Ta}_{48}\text{O}_{119}$m, and c) $a\text{Ta}_{48}\text{O}_{119}$h. In (a–c), the transmission for stoichiometric $a\text{Ta}_{48}\text{O}_{120}$ is shown in dashed red lines for comparison. Transmission paths are depicted in (d) for $a\text{Ta}_{48}\text{O}_{119}$l and in (e) for $a\text{Ta}_{48}\text{O}_{119}$m. In (d) and (e), red and blue balls denote O and Ta, respectively; Ta atoms that are the nearest neighbor to V_O are shown as large brown balls. The blue arrows are for forward transmission and the red for backward transmission. The arrow's thickness is proportional to the transmission amplitude. For clarity, electron transmission paths without the atomic structures are shown in the right panels of (d) and (e).

respectively, indicating larger transport efficiency from $a\text{Ta}_{48}\text{O}_{119}$l, $a\text{Ta}_{48}\text{O}_{119}$m, to $a\text{Ta}_{48}\text{O}_{119}$h. The resistivity R for $a\text{Ta}_{48}\text{O}_{119}$ (0.8% V_O) was calculated as 1.28×10^{15}, 5.17×10^{7}, and 2.07×10^{4} μΩ cm for $a\text{Ta}_{48}\text{O}_{119}$l, $a\text{Ta}_{48}\text{O}_{119}$m, and $a\text{Ta}_{48}\text{O}_{119}$h, respectively. Measured resistivities of TaO_x by a recent experiment were 9.1×10^{11}, 1.2×10^{10}, 4.5×10^{5}, and 7.4×10^{4} μΩ cm

© 2022 The Authors. Advanced Electronic Materials published by Wiley-VCH GmbH

2199160x, 2023, 1, Downloaded from https://onlinelibrary.wiley.com/doi/10.1002/aelm.202200828, Wiley Online Library on [26/07/2023]. See the Terms and Conditions (https://onlinelibrary.wiley.com/terms-and-conditions) on Wiley Online Library for rules of use; OA articles are governed by the applicable Creative Commons License

for 0%, 14%, 25%, and 42% V_O, which could be a statistical average over measurements.[16] The measured large resistivity for V_O < 10% is thus qualitatively consistent with the predicted larger resistivity for $a Ta_{48}O_{119}l$. The resistivity for $a Ta_{48}O_{119}m$ and $a Ta_{48}O_{119}h$ is significantly lower compared to $a Ta_{48}O_{119}l$, as expected, where the resistivity of $a Ta_{48}O_{119}h$ is on the same order of the measured resistivity for 40% V_O.[16]

The relatively lower and higher transport efficiency in $a Ta_{48}O_{119}l$ versus $a Ta_{48}O_{119}m$ is consistent with the transmission paths of the defect transmission channels. The results in Figure 2a,b show new channels in the transmission gap in $a Ta_{48}O_{119}l$ and $a Ta_{48}O_{119}m$ (black lines) as compared to $a Ta_{48}O_{120}$ (red line). These channels originate from the single vacancy in $a Ta_{48}O_{119}l$ and $a Ta_{48}O_{119}m$, namely so-called defect transmission channels. Since the defect transmission channels assume the characteristics of the vacancy, its transmission paths will reveal the scattering behavior of the defect structures. Thus, we chose these channels to discern the different transport characteristics in $a Ta_{48}O_{119}l$ versus $a Ta_{48}O_{119}m$. In the transmission paths, the transmission coefficient $T(E)$ is split into $T_{ij}(E)$ local bond contributions.[35] A positive value of T_{ij} is visualized as an arrow from i to j, and a negative value from j to i. A negative value corresponds to backscattering along the bond. The transmission path for the defect channel at $E = -0.69$ eV for $a Ta_{48}O_{119}l$ is shown in Figure 2d, where three Ta atoms surrounding the vacancy form a trimer and the forward transport path from left to right (in blue) splits into two. One of the paths continues to the end of the scattering region, comprising the major forward path, but the second path is weak in transmission and comprises a minor forward path. Backscattering occurs at the Ta atoms neighboring V_O, leading to a backward path (in red). The backward path and the major forward path form a loop, and although there is net transmission forward from left to right, it is weak, so that there is a relatively small probability for electron traveling from left to right through the material. On the other hand, in the transmission path for the defect channel at $E = -0.18$ eV for $a Ta_{48}O_{119}m$ (Figure 2e), two forward paths from left to right are illustrated, and backscattering does not lead to a backward path. Thus, while the electron transmission in a path forward is partially cancelled by a weak backward transmission path for $a Ta_{48}O_{119}l$, the higher transmission efficiency for $a Ta_{48}O_{119}m$ stems from two forward electron transmission paths and no backward path. Close examination of the local amorphous structure reveals that in $a Ta_{48}O_{119}l$ a Ta trimer rather than a dimer surrounds V_O, which could inhibit the transmission to some extent. The local amorphous structure determines the electron scattering behavior, resulting in an increased number of transmission paths in the higher conducting $a T_{48}O_{119}$, highlighting the importance of understanding the local amorphous structure.

To understand the effects of varying the V_O concentration in TaO_x, we consider $a Ta_{48}O_{96}$ and $a Ta_{48}O_{84}$. Multiple vacancy states in the energy gap for $a Ta_{48}O_{96}$ are indicated in the −2.5 to 0 eV energy region (see density of states [DOS] in **Figure 3**a), and band decomposed charge densities for the vacancy bands show the V_O distribution (Figure 3b,c). Correspondingly, Figure 3d shows the DOS for $a Ta_{48}O_{84}$, where the vacancy states are in the −2.9 to 0 eV energy region, and the vacancy band-decomposed charge densities are depicted in Figure 3e,f. As discussed below, V_O filaments contribute to the transmission paths at 0.2 V bias for $a Ta_{48}O_{96}$ and $a Ta_{48}O_{84}$ (black ovals in Figure 3b,c,e,f). The illustration of the dominant paths in the upper region comprising of V_O is depicted by brown Ta atoms neighboring oxygen vacancies, as determined from the oxygen vacancy locations for $a Ta_{48}O_{96}$ (Figure 3b,c) and $a Ta_{48}O_{84}$ (Figure 3e,f).

In amorphous TaO_x, e.g., $a Ta_{48}O_{96}$ and $a Ta_{48}O_{84}$, V_O accumulate and assemble, while in a crystalline structure, extended oxygen vacancies would typically comprise of specific structures (e.g., see ref. [21]). Indeed, spherical-like filaments of different sizes were recently observed.[16] The estimated filament cross sections for $Ta_{48}O_{96}$ and $a Ta_{48}O_{84}$ (Figure 3) are about 5.3 and 6.4 Å, namely 30–50% of the supercell length. These relatively large filament cross sections in model system calculations could explain, in part, observed large filament cross sections, for example, 100 nm in Ta_2O_5-based memristive devices.[16] Our results quantify an approach for analysis of the effects sub-stoichiometry on the electron transport, where the interplay with the amorphous oxide structure has to be considered as well.

The transmission under a bias of 0.2 V for $a Ta_{48}O_{96}$ and $a Ta_{48}O_{84}$ is shown in **Figure 4**. A peak near zero for $a Ta_{48}O_{96}$ in the energy region between the Fermi energy of the left (ε_F^L) and right electrode (ε_F^R) has transmission of 2.3 × 10^{-3} (Figure 4a) and current of 7.4 nA. The transmission at 0.2 V for $a Ta_{48}O_{84}$ for the peak near energy zero between ε_F^L and ε_F^R (Figure 4b) has transmission of 3.5 × 10^{-2} and current of 117.6 nA. At finite bias, electrons with energies in the bias window, specifically for $\varepsilon_F^L \le E \le \varepsilon_F^R$ at an electron temperature of 300 K, give rise to electric current.[36] Thus, in the transmission spectra in Figure 4a,b only the transmission peaks between the two dashed lines contribute to the current. Studying the transmission eigenstate at the peak, it (Figure 4c) demonstrates that the state density decays from left to right, as expected, with the dominant transmission path in the upper region at the right-hand side of Figure 4c, generated by oxygen vacancies. Similarly, for $a Ta_{48}O_{84}$, the state density decays from left to right (Figure 4d). Note that Ta atoms neighboring oxygen vacancies tend to shorten the Ta–Ta distance. Values of the calculated resistivity (300 K electron electrode temperature) for $a Ta_{48}O_{96}$ (20% Vo) and $a Ta_{48}O_{84}$ (30% Vo) were 4.2 × 10^4 and 7.9 × 10^3 μΩ cm, respectively, which are comparable to the measured resistivity values of 4.5 × 10^5 and 7.4 × 10^4 μΩ cm for TaO_x thin films with 25% and 42% Vo concentration, respectively.[16] The calculated resistivities are smaller than measured values, which could be due to the simulated representative amorphous structures from MD samples. Statistical averages over MD samples would potentially improve the agreement with experiment.

As the device is switched between the HRS and LRS states through changes in the stoichiometry, we also used the structures $a Ta_{48}O_{96}$ (20% Vo) and $a Ta_{48}O_{119}m$, which represens an averaged resistivity of the $a Ta_{48}O_{119}$ (0.8% Vo) structures, enabling to model the resistivity of the high-resistance and low-resistance states, respectively. Experimentally, it was found that resistive switching leads to the formation of a conductive filament with an oxygen vacancy concentration of about 20%.[16] The resistivity ratio between $a Ta_{48}O_{119}m$ and $a Ta_{48}O_{96}$ is $5.17 \times 10^7 / 4.2 \times 10^4 = 1.23 \times 10^3$, in agreement with the measured value between

© 2022 The Authors. Advanced Electronic Materials published by Wiley-VCH GmbH

2199160x, 2023, 1, Downloaded from https://onlinelibrary.wiley.com/doi/10.1002/aelm.202200828, Wiley Online Library on [26/07/2023]. See the Terms and Conditions (https://onlinelibrary.wiley.com/terms-and-conditions) on Wiley Online Library for rules of use; OA articles are governed by the applicable Creative Commons License

2199160x, 2023, 1, Downloaded from https://onlinelibrary.wiley.com/doi/10.1002/aelm.202200828, Wiley Online Library on [26/07/2023]. See the Terms and Conditions (https://onlinelibrary.wiley.com/terms-and-conditions) on Wiley Online Library for rules of use; OA articles are governed by the applicable Creative Commons License

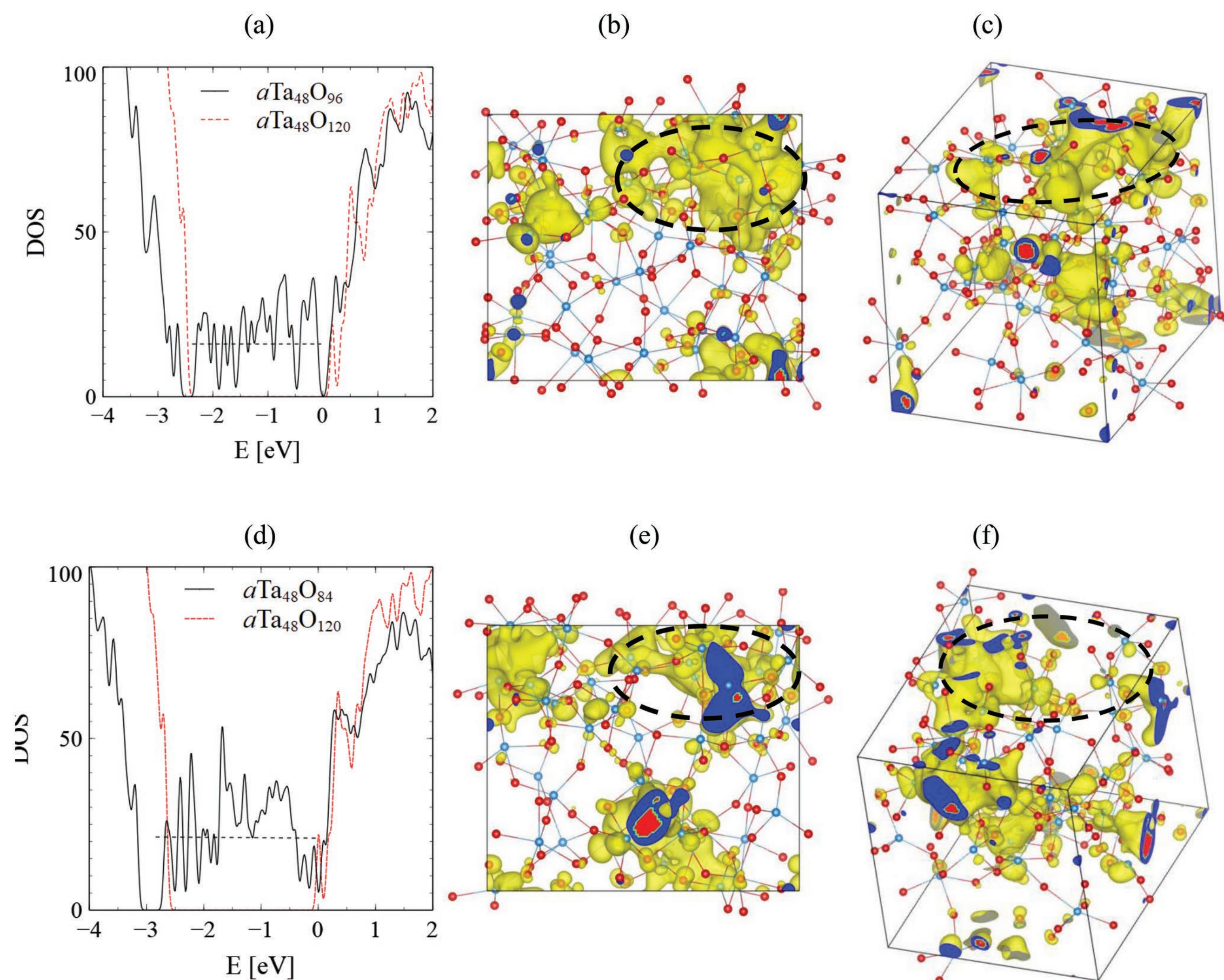

Figure 3. aTa$_{48}$O$_{96}$ and aTa$_{48}$O$_{84}$: DOS in (a) and (d), as well as vacancy band decomposed charge densities in (b) and (e)—top view and (c) and (f)—side view, respectively. In (a) and (d), DOS for aTa$_{48}$O$_{120}$ are in dashed red lines and the DOS from vacancies in black dashed lines. In (b,c) and (e,f), a dashed black oval indicates an oxygen vacancy region.

the HRS and LRS states (≈10^3) for the programmed graphene/Ta$_2$O$_5$/Ta device.[16]

With the inclusion of a scavenging Ta layer or a TiN electrode directly, we investigated the interfaces between the Ta$_2$O$_5$ surface along the z-axis and the Ta[100] and TiN[100] surfaces. Experimentally, Ta[100] is a stable metal surface,[37] while DFT calculations on TiN indicated that TiN[100] is the most stable and TiN[111] the least stable surface.[38] Nonetheless, TiN-based electrodes and gate contacts are typically polycrystalline, whose constituting grains have different sizes and expose multiple facets, which depend on the conditions and techniques used to grow the sample.[39] Here, we chose the Ta[100] and TiN[100] surfaces to minimize the strain at the interface. To build the interface, we generated slabs of Ta[100] and TiN[100] with four layers, as well as a unit cell of a Ta$_2$O$_5$ slab, considering both crystalline and amorphous structures, that is, cTa$_{48}$O$_{120}$ and aTa$_{48}$O$_{120}$. A vacuum region was added perpendicular to the interface to avoid image interactions. Initial interface structures indicated lattice mismatch values of 3.5%, 1.9%, 4.5%, and 1.9% for cTa$_{48}$O$_{120}$/Ta, cTa$_{48}$O$_{120}$/TiN, aTa$_{48}$O$_{120}$/Ta, and aTa$_{48}$O$_{120}$/TiN, respectively. The crystalline interfaces were then optimized by DFT, while ab initio MD followed by DFT was employed for the amorphous interfaces. The atom-relaxation region included two layers of the metal surface and for the crystalline interface a layer of the cTa$_{48}$O$_{120}$ surface.

In analyzing the optimized structures, we note that for the cTa$_{48}$O$_{120}$/Ta interface, oxygen atoms from cTa$_{48}$O$_{120}$ form O−Ta bonds to the Ta surface and similarly to the TiN interface, forming O−Ti bonds. Simulations for aTa$_{48}$O$_{120}$/Ta led to oxygen diffusion from aTa$_{48}$O$_{120}$ to the Ta surface, and some Ta diffusion from the Ta surface to aTa$_{48}$O$_{120}$ (see Figure S6a, Supporting Information). These results were qualitatively reproduced by empirical MD (not shown), but the ab initio MD simulations showed enhanced atom migration. The diffused oxygen atoms prefer interstitial positions on the Ta surface, generating oxygen vacancies in aTa$_{48}$O$_{120}$, while Ta diffusion causes Ta

© 2022 The Authors. Advanced Electronic Materials published by Wiley-VCH GmbH

ADVANCED ELECTRONIC MATERIALS
www.advelectronicmat.de

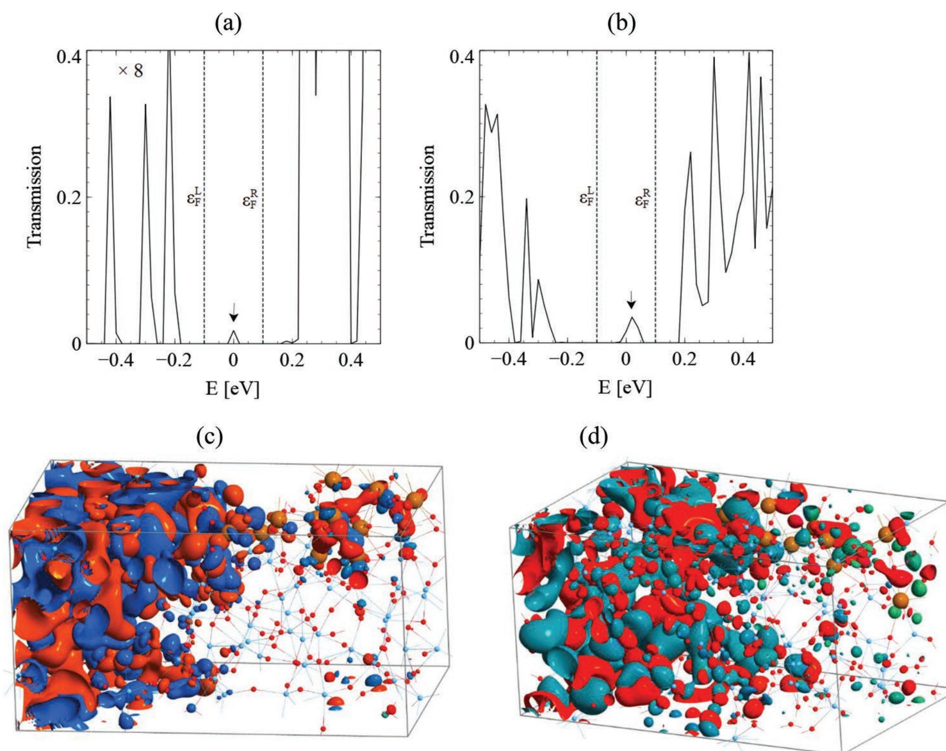

Figure 4. Transmission upon 0.2 V applied bias for a) $a\text{Ta}_{48}\text{O}_{96}$ and b) $a\text{Ta}_{48}\text{O}_{84}$. Transmission eigenstates for the transmission channel ($E = 0$ eV for $a\text{Ta}_{48}\text{O}_{96}$ and 0.02 eV for $a\text{Ta}_{48}\text{O}_{84}$) in the bias window for c) $a\text{Ta}_{48}\text{O}_{96}$ and d) $a\text{Ta}_{48}\text{O}_{84}$. On the main transmission paths, brown balls denote Ta atoms neighboring oxygen vacancies. The transmission is 2.3×10^{-3} for (c) and 3.5×10^{-2} for (d).

accumulation at the $a\text{Ta}_{48}\text{O}_{120}$ side. Similarly, for the $a\text{Ta}_{48}\text{O}_{120}$/TiN interface, the simulations led to Ta and O diffusion from $a\text{Ta}_{48}\text{O}_{120}$ to TiN, and diffusion of Ti and N atoms from TiN to $a\text{Ta}_{48}\text{O}_{120}$ (Figure S6b, Supporting Information). This diffusion causes substitution of Ti by Ta and N by O in TiN. Note that the diffusion of Ti and N into $a\text{Ta}_{48}\text{O}_{120}$ could be reduced, and thus the Ta scavenging layer would promote V_O filament generation. We note that classical MD simulations were previously employed to study oxygen diffusion in amorphous stoichiometric tantalum oxide[40] and found an activation energy of 1.55–1.60 eV in relatively good agreement with experiment, confirming relative facile diffusion, lower than in the crystalline structure.

To gain insight into the effect of the interface on the transport efficiency, the optimized interfaces were used to build junction system models, consisting of a left electrode of $c\text{Ta}_{48}\text{O}_{120}$ or $a\text{Ta}_{48}\text{O}_{120}$, a right electrode of Ta[100] or TiN[100], and a central scattering region that includes the left electrode extension, the right electrode extension, and the $c\text{Ta}_{48}\text{O}_{120}$/Ta[100] and $c\text{Ta}_{48}\text{O}_{120}$/TiN[100] interfaces or the $a\text{Ta}_{48}\text{O}_{120}$/Ta[100] and $a\text{Ta}_{48}\text{O}_{120}$/TiN[100] interfaces (see Figure S7a–d, Supporting Information). We indicate in Figure S7c, Supporting Information, the left and right electrodes and central region, and the left and right electrode extensions in the central region. The local DOS (LDOS) at zero bias in the central region for these interface model systems are shown in **Figure 5**, where the band structure of the insulating layer of $c\text{Ta}_{48}\text{O}_{120}$ and $a\text{Ta}_{48}\text{O}_{120}$ is on the left-hand side and that of the metal on the right-hand side. The band gap is indicated by the black area (no DOS), bounded by the valence band maximum (VBM) and the conduction band minimum (CBM) in the LDOS for each interface. We find that due to charge transfer at the interface the bands of $\text{Ta}_{48}\text{O}_{120}$ are bent down toward the $\text{Ta}_{48}\text{O}_{120}$/metal interface, resulting in small or negligible electron Schottky barriers (0.8 eV for $c\text{Ta}_{48}\text{O}_{120}$/TiN and nearly 0 for the other cases), indicating Ohmic contacts. Here, the band bending magnitude Φ can be defined as the energy difference between the VBM at the $\text{Ta}_{48}\text{O}_{120}$ extension and at the interface. Electrons are transferred from the metal to $\text{Ta}_{48}\text{O}_{120}$, and local fields at the interface cause the bending down of the $\text{Ta}_{48}\text{O}_{120}$ bands. The $c\text{Ta}_{48}\text{O}_{120}$/Ta, $a\text{Ta}_{48}\text{O}_{120}$/Ta, and $a\text{Ta}_{48}\text{O}_{120}$/TiN interfaces indicate a similar Φ, while $c\text{Ta}_{48}\text{O}_{120}$/TiN has a smaller Φ (see Figure 5). The predicted Ohmic contact at the $a\text{Ta}_{48}\text{O}_{120}$/Ta interface agrees with observations for a graphene/Ta_2O_5/Ta device, where the low work function of the Ta electrode forms an Ohmic contact to the Ta_2O_5 switching layer, whereas the high work function-graphene electrode forms a Schottky barrier.[16]

The system's Fermi level is near the center of the band gap in the $\text{Ta}_{48}\text{O}_{120}$ extension. If $\text{Ta}_{48}\text{O}_{120}$ is n-doped, the Fermi level will shift up closer to the $\text{Ta}_{48}\text{O}_{120}$ CBM, and the corresponding electron Schottky barrier will be zero. If $\text{Ta}_{48}\text{O}_{120}$ is p-doped, the Fermi level will shift down closer to the VBM and the corresponding hole Schottky barrier will be about Φ. Experimentally, a small Schottky barrier of 0.75 eV was measured for the Ta_2O_5/Ta interface.[41] The measured finite Schottky barrier due to Fermi level pinning could be caused by the complexity at the interface in a realistic system, for example, a combination of crystallographic facets and defects at the surfaces. From the transmission spectra at zero bias, energy barriers of 1.0 and

© 2022 The Authors. Advanced Electronic Materials published by Wiley-VCH GmbH

2199160x, 2023, 1, Downloaded from https://onlinelibrary.wiley.com/doi/10.1002/aelm.202200828, Wiley Online Library on [26/07/2023]. See the Terms and Conditions (https://onlinelibrary.wiley.com/terms-and-conditions) on Wiley Online Library for rules of use; OA articles are governed by the applicable Creative Commons License

2199160x, 2023, 1, Downloaded from https://onlinelibrary.wiley.com/doi/10.1002/aelm.202200828, Wiley Online Library on [26/07/2023]. See the Terms and Conditions (https://onlinelibrary.wiley.com/terms-and-conditions) on Wiley Online Library for rules of use; OA articles are governed by the applicable Creative Commons License

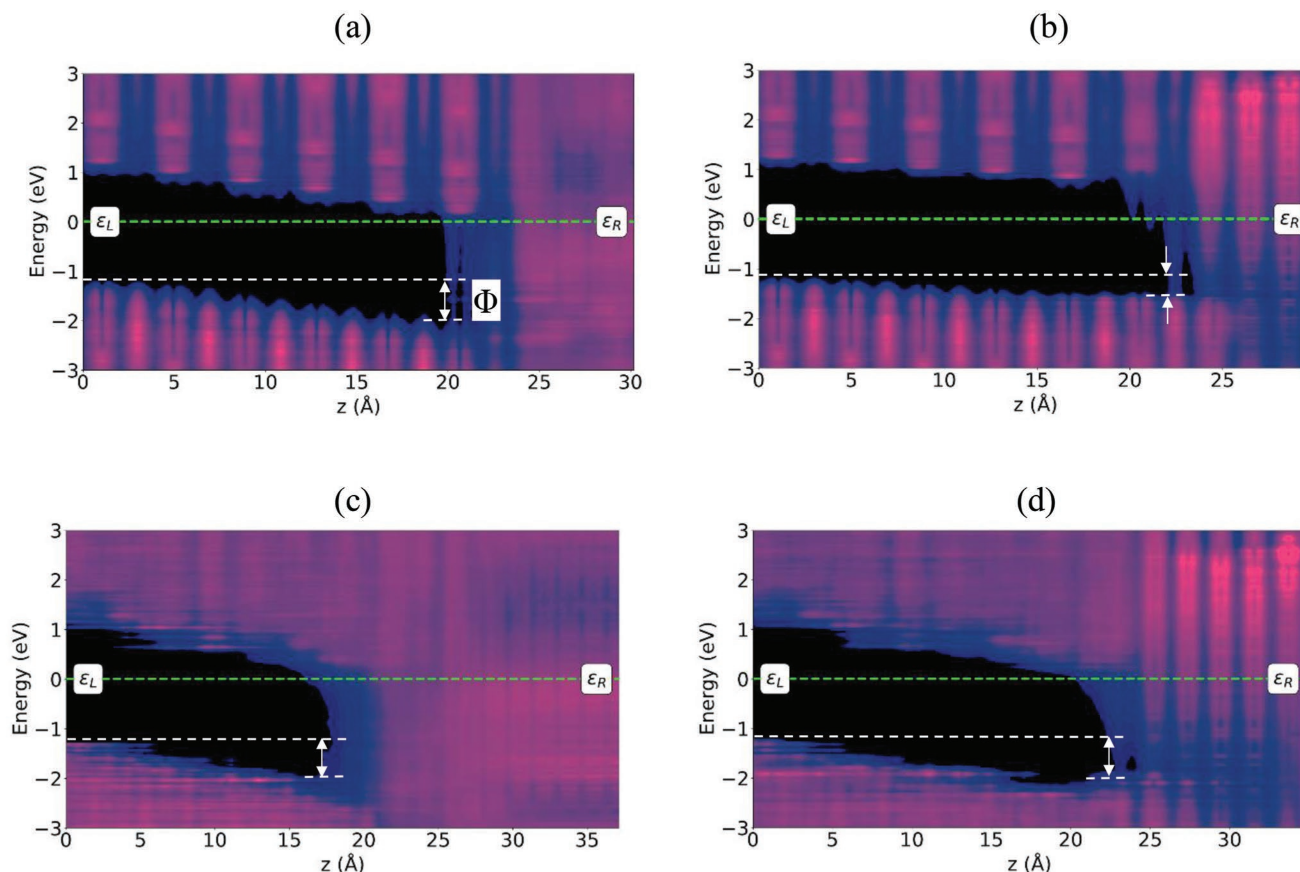

Figure 5. LDOS at the central region of a) $c\text{Ta}_{48}\text{O}_{120}$/Ta[100], b) $c\text{Ta}_{48}\text{O}_{120}$/TiN[100], c) $a\text{Ta}_{48}\text{O}_{120}$/Ta[100], and d) $a\text{Ta}_{48}\text{O}_{120}$/TiN[100] junctions.

0.36 eV for $c\text{Ta}_{48}\text{O}_{120}$/Ta and $c\text{Ta}_{48}\text{O}_{120}$/TiN, and of 0.61 and 0.81 eV for $a\text{Ta}_{48}\text{O}_{120}$/Ta and $a\text{Ta}_{48}\text{O}_{120}$/TiN, respectively, were calculated (see Figure S8a,b, Supporting Information). The energy barrier in the valence band causes stronger quenching of the transmission than in the conduction band, inducing electron and hole asymmetry in the transmission. Correspondingly, the interfaces quench the conductance more at the valence band than at the conduction band (see Figure S8c,d, Supporting Information). Our results indicate that transport efficiency improvements by oxygen vacancies at the amorphous interfaces are caused by atomic diffusion. We also notice that upon a Ta layer inclusion, the amorphous interface tends to reduce the energy barrier (1.0 vs 0.62 eV for $c\text{Ta}_{48}\text{O}_{120}$/Ta vs $a\text{Ta}_{48}\text{O}_{120}$/Ta, respectively) and thus decrease the contact resistance. We find that V_O generation and Ta accumulation at the interface of $a\text{Ta}_{48}\text{O}_{120}$/Ta could be consistent with a recent analysis.[42] Upon replacing $a\text{Ta}_{48}\text{O}_{120}$ (no vacancy) by $a\text{Ta}_{48}\text{O}_{96}$ (20% V_O) or $a\text{Ta}_{48}\text{O}_{96}$ (30% V_O), the oxygen vacancies in amorphous TaO_x are expected to diffuse toward the interface, which further increases the number of vacancies at the interface. Therefore, the band is expected to be bent further, which reduces contact resistance for electron transport. The Schottky barrier for electron transport is nearly zero for the $c\text{Ta}_{48}\text{O}_{120}$/Ta, $a\text{Ta}_{48}\text{O}_{120}$/Ta, and $a\text{Ta}_{48}\text{O}_{120}$/TiN interfaces, and about 0.8 eV for $c\text{Ta}_{48}\text{O}_{120}$/TiN interface. As a result, electron transport in the former interfaces is over the barrier, while for the latter interface electron transport through tunneling at low bias occurs. On the other hand, the energy barrier for the hole has a finite but a small value for the four interfaces. The transport across the interfaces is through tunneling at low bias, and over the barrier at a relatively high bias.

3. Conclusions

In summary, to gain atomic-level insight into the filament conduction mechanism of TaO_x thin films upon sub-stoichiometry, we report on a theoretical characterization of EEL spectra, where both crystalline and amorphous TaO_x model systems were considered. In employing the many-body GW method for cTa and $c\text{Ta}_2\text{O}_5$ we demonstrate, encouragingly, agreement with our EELS profile measurements, which enabled benchmarking calculations for amorphous structures by DFT. Our results for the amorphous model structures, including varying percentages of oxygen vacancies, are consistent with our experimental data, and moreover demonstrate the potential applicability of EELS to characterize the oxygen vacancy concentration in filaments due to the blue-shift with increased sub-stoichiometry. For a given V_O, we show decrease in the resistivity due to changes in the local amorphous structure, for example, from a Ta trimer to a dimer surrounding the vacancy, thus affecting the electron transmission path. In modeling the effects of an

 © 2022 The Authors. Advanced Electronic Materials published by Wiley-VCH GmbH

2199160x, 2023, 1, Downloaded from https://onlinelibrary.wiley.com/doi/10.1002/aelm.202200828, Wiley Online Library on [26/07/2023]. See the Terms and Conditions (https://onlinelibrary.wiley.com/terms-and-conditions) on Wiley Online Library for rules of use; OA articles are governed by the applicable Creative Commons License

increased number of oxygen vacancies, we find initiation of filaments in the amorphous structures through vacancy assembly, consistent with transmission calculations at low bias. Modeling the interface with a Ta scavenging layer or directly with the TiN electrode as based on interface systems for crystalline and amorphous model systems derived by ab initio MD simulations, indicates oxygen vacancy generation and Ta accumulation at the interface through atom diffusion, showing that a Ta cluster-based mechanism in filament conduction cannot be ruled out at such an interface. Our results provide a basis for investigating effects of sub-stoichiometry on filament formation in thin film TaO_x memristive devices.

4. Experimental Section

Computational Details: DFT calculations were performed with the Vienna ab initio simulation package,[43,44] applying the projector augmented-wave potential. The Kohn–Sham equations were solved using a plane wave basis set, with an energy cutoff of 420 eV. The Perdew–Burke–Ernzerhof (PBE) exchange-correlation functional was used[45] unless indicated otherwise. All atomic geometries were fully relaxed until forces were less than 0.01 eV Å^{-1}. A Gaussian smearing width of 0.05 eV was used for k space integrals. k-point samplings of 15 × 15 × 15, 6 × 6 × 10, and 3 × 3 × 3 were employed for the Ta, Ta_2O_5, and $a Ta_{48}O_{120-x}$, as based on a previous work,[24] respectively. The range-separated HSE06 functional[46,47] was employed in the electronic structure calculations to account for the PBE underestimation of the $Ta_{48}O_{120-x}$ band gap predictions.

The DFT optimized cTa primitive cell was based on the stable α-Ta phase with a body-centered cubic crystal structure, shown in Figure S1a, Supporting Information. The calculated lattice constant of 3.3276 Å was in agreement with the measured value of 3.3057 Å.[48] For the crystal structure of Ta_2O_5 (cTa_2O_5), the previously suggested model was used,[49] where the building blocks of the orthorhombic structure were octahedral TaO_6 and pentagonal bipyramidal TaO_7 polyhedra. The DFT optimized cTa_2O_5 unit cell (Figure S1b, Supporting Information) had cell dimensions of 7.41, 6.26, and 3.93 Å, consistent with previous work with values of 7.13, 6.03, and 3.82 Å.[49] For amorphous $Ta_{48}O_{120-x}$ (Figure S1c–h, Supporting Information), previous structures derived by ab initio MD and DFT were used.[24] To model sub-stoichiometric tantalum oxide, structures with neutral vacancies were considered, specifically $aTa_{48}O_{119}$ (0.8% V_O), namely $aTa_{48}O_{119}$l, $aTa_{48}O_{119}$m, and $aTa_{48}O_{119}$h, which represent low, medium, and high electric conductivity, respectively.[24] Structures from ref. [24] were used for multiple-oxygen vacancy systems as well, specifically $aTa_{48}O_{96}$ (20% V_O) and $aTa_{48}O_{84}$ (30% V_O).

The imaginary part of the interband dielectric function was given by the Cartesian tensor[50] as

$$\varepsilon_{\alpha\beta}^{2,\mathrm{inter}}(\omega)=\frac{4\pi^2e^2}{\Omega}\lim_{q\to 0}\frac{1}{q^2}\sum_{c,v\vec{k}}2\omega_{\vec{k}}\delta\left(\varepsilon_{c\vec{k}}-\varepsilon_{v\vec{k}}-\omega\right)\times\left\langle u_{c\vec{k}+\vec{e}_\alpha q}\middle|u_{v\vec{k}}\right\rangle\left\langle u_{c\vec{k}+\vec{e}_\beta q}\middle|u_{v\vec{k}}\right\rangle^* \tag{1}$$

where ω was in units of energy; Ω the volume of the cell; $\vec{e}$ unit vectors for the three Cartesian directions; c and v referred to conduction and valence states, respectively; $u_{c\vec{k}}$ were the cell-periodic orbitals at $\vec{k}$. In the calculation of $\varepsilon_{\alpha\beta}^{2,\mathrm{inter}}$, $\vec{k}$ was restricted to the irreducible wedge of the first Brillouin zone. The real part of the interband dielectric tensor was obtained from Kramers–Kronig transformation[51,52] given by

$$\varepsilon_{\alpha\beta}^{1,\mathrm{inter}}(\omega)=1+\frac{2}{\pi}P\int_0^\infty\frac{\varepsilon_{\alpha\beta}^{2,\mathrm{inter}}(\omega')\omega'}{\omega'^2+\omega^2+i\eta}d\omega' \tag{2}$$

where P denoted the principal value of the integral.

The imaginary part of the intra-band dielectric function ($\varepsilon^{\mathrm{intra}}=\varepsilon^{1,\mathrm{intra}}+i\varepsilon^{2,\mathrm{intra}}$) was given by[53]

$$\varepsilon_{\alpha\beta}^{2,\mathrm{intra}}(\omega)=\frac{\bar{w}_{\alpha\beta}^2\cdot\Gamma}{\omega\cdot\left(\omega^2+\Gamma^2\right)} \tag{3}$$

and the real part by

$$\varepsilon_{\alpha\beta}^{1,\mathrm{intra}}(\omega)=-\frac{\bar{w}_{\alpha\beta}^2}{\omega^2+\Gamma^2} \tag{4}$$

where Γ was damping factor. $\Gamma\to 0$ and $\bar{W}$ was the plasma frequency, namely

$$\bar{w}_{\alpha\beta}^2=\frac{4\pi e^2}{\Omega\hbar^2}\sum_{n,\vec{k}}2g_{\vec{k}}\frac{\partial f\left(\varepsilon_{n\vec{k}}\right)}{\partial\varepsilon}\left(\vec{e}_\alpha\frac{\partial\varepsilon_{n\vec{k}}}{\partial\vec{k}}\right)\left(\vec{e}_\beta\frac{\partial\varepsilon_{n\vec{k}}}{\partial\vec{k}}\right) \tag{5}$$

where $f(\varepsilon_{n\vec{k}})$ was the DFT occupation number and $g_{\vec{k}}$ was the weighting factor, accounting for the summation performed only over the irreducible part of the Brillouin zone, summing to unity. The total dielectric function was expressed as $\varepsilon=\varepsilon^{\mathrm{intra}}+\varepsilon^{\mathrm{inter}}=\varepsilon^1+i\varepsilon^2$.

The EELS was calculated by

$$L_{ij}(\omega)=Im\left(\frac{-1}{\varepsilon_{ij}(\omega)}\right)=\frac{\varepsilon^2}{\left[\varepsilon^1\right]^2+\left[\varepsilon^2\right]^2} \tag{6}$$

where $i,j=x,y,z$. An average value was taken, defined by

$$L=\left(L_{xx}+L_{yy}+L_{zz}\right)/3 \tag{7}$$

To improve the accuracy in the calculation of EELS, the many-body GW method was employed for crystalline cTa and cTa_2O_5.

Electron transport modeling was carried out with the non-equilibrium Green's function formalism combined with DFT, based on the Landauer–Buttiker approach,[56] previously implemented by Brandbyge et al.[57] In a simulated device, the system was divided into a left (L) electrode, central region, and right (R) electrode. Under an applied bias (V_b), the chemical potential in each electrode shifted as

$$\mu_L(V_b)=\mu_L(0)+\frac{eV_b}{2}\ \mathrm{and}\ \mu_R(V_b)=\mu_R(0)-\frac{eV_b}{2} \tag{8}$$

where $\mu_L(0)$ and $\mu_R(0)$ were the chemical potentials at zero bias for the L and R electrodes, respectively. The transmission was given as a function of the energy E and bias V_b

$$T(E,V_b)=Tr\left[\Gamma_L(E,V_b)G^R(E)\Gamma_R(E,V_b)G^A(E)\right] \tag{9}$$

G^R and G^A were the retarded and advanced Green's functions, respectively; Γ was the contact broadening for the electrodes. The current was calculated from the transmission by

$$I(V_b)=\frac{2e}{h}\int_{\mu_L(V_b)}^{\mu_R(V_b)}T(E,V_b)\left[f(E,\mu_L)-f(E,\mu_R)\right]dE \tag{10}$$

The conductance was calculated by

$$\sigma(T_L)=\frac{2e^2}{h}\int T(E)f'(\eta(E))\frac{dE}{k_bT_R} \tag{11}$$

where T_L (T_R) was the electron temperature (here $T_L=T_R$), and

© 2022 The Authors. Advanced Electronic Materials published by Wiley-VCH GmbH

$$f'(\eta(E)) = f'\left(\frac{E - E_F^L}{k_b T_R}\right) \tag{12}$$

the derivative of the Fermi function. Assuming that the effect of the gate potential was a shift of the relative positions of the electrode Fermi levels in the transmission, conductance as a function of the gate potential (or energy) was calculated by linear response theory. The transmission per spin is reported. Calculations were performed with the Quantum Atomistix Toolkit (ATK) program,[36,58] using the PBE functional[45] and FHI pseudopotential,[59] with a double-ζ polarization basis set for all atoms. A density mesh cut-off of 75 Ha for grid integration was used. Dirichlet boundary conditions were used in the transport direction and periodic boundary conditions in the other two directions, employing a Poisson solver.

To model the amorphous interfaces by ab initio MD, a melt-and-cooling approach[24,26] was used at a NVT ensemble using the Nosé–Hoover thermostat with a Nosé mass of 2.0. 300 eV cutoff energies, Γ-point sampling, 3 fs step intervals. An energy convergence tolerance of 1×10^{-3} eV was used at each MD step in the simulations. The initial $a\mathrm{Ta_{48}O_{120}}$/Ta ($a\mathrm{Ta_{48}O_{120}}$/TiN) structure was first sustained at 3900 K for 11.7 ps for melting, and subsequently equilibrated in the relaxation region. The structure was then cooled to 300 K using a 2 ps stepwise protocol, resulting in a cooling rate of 150 K $\mathrm{ps^{-1}}$ for 12 steps, subsequently optimized at the DFT level. For comparison, MD with an empirical force-field was also performed, with an NVT ensemble and Langevin thermostat for the annealing process and Nosé–Hoover thermostat for the cooling process. The initial $a\mathrm{Ta_{48}O_{120}}$/Ta structure was sustained for 50 ps at 3900 K, and subsequently cooled to 300 K using a continuous cooling procedure with a cooling rate of 14 K $\mathrm{ps^{-1}}$, then optimized by the modified embedded atom method potential[60] in ATK.[36,58]

Experimental Synthesis and Characterization: Amorphous TiN/Ta/$\mathrm{TaO_x}$/TiN films were grown using reactive PDV in Sandia's MESAFab, using a process similar to that described in. ref. [34]. In this case, deposition was performed at the high oxygen pressure end of the spectrum, creating stoichiometric films as deposited. However, it was expected that some of the oxygen was gettered from the film due to the adjacent Ta layer. Reactive sputtering was used to fabricate $\mathrm{TaO_x}$-based memristor stacks[34] that consisted of a TiN bottom electrode, a $\mathrm{TaO_x}$ layer, a Ta layer, and a TiN top electrode, all sputter-deposited on top of a blanket tungsten layer. The TiN/Ta/$\mathrm{TaO_x}$/TiN stack was deposited in two separate chambers of the physical vapor deposition tool without breaking vacuum. A warm-up wafer was run between those two depositions in order to condition the chamber prior to depositing each different film. Figure S2a, Supporting Information, shows a high angle annular dark-field imaging-scanning transmission electron microscopy image wherein the individual layers in the device region were identified, including a Ta scavenging layer. An examination of the overall structure by elemental mapping by energy-dispersive X-ray spectrum imaging, shown in Figure S2b, Supporting Information, clearly demarcated the top and bottom electrodes corresponding to the Ti rich regions, and the memristor/exchange layers corresponding to the Ta and O regions. Analysis of the individual elemental line profiles (obtained from summed counts parallel to the interfaces) is shown in Figure S2c, Supporting Information, revealing that the O-profile was nearly constant at the memristor region and was graded (as intended) in the getter region.

Supporting Information

Supporting Information is available from the Wiley Online Library or from the author.

Acknowledgements

The authors acknowledge helpful support and resources from the DoD High-Performance Computing Modernization Program, and financial support from the Air Force Research Laboratory Commander's Research and Development Funding Program. Work performed at the Molecular Foundry was supported by the Office of Science, Office of Basic Energy Sciences, of the U.S. Department of Energy under contract number DE-AC02-05CH11231.

Conflict of Interest

The authors declare no conflict of interest.

Data Availability Statement

The data that support the findings of this study are available from the corresponding author upon reasonable request.

Keywords

conducting filaments, density functional theory, electron energy loss spectrum, electron transport, memristors, thin film $\mathrm{TaO_x}$

Received: August 1, 2022
Revised: September 7, 2022
Published online: October 20, 2022

[1] D. B. Strukov, G. S. Snider, D. R. Stewart, R. S. Williams, *Nature* **2008**, *453*, 80.
[2] L. Chua, *IEEE Trans. Circuit Theory* **1971**, *18*, 507.
[3] J. J. Yang, M. D. Pickett, X. Li, D. A. Ohlberg, D. R. Stewart, R. S. Williams, *Nat. Nanotechnol.* **2008**, *3*, 429.
[4] R. Waser, R. Dittmann, G. Staikov, K. Szot, *Adv. Mater.* **2009**, *21*, 2632.
[5] D. Ielmini, *Semicond. Sci. Technol.* **2016**, *31*, 063002.
[6] Z. Wang, H. Wu, G. W. Burr, C. S. Hwang, K. L. Wang, Q. Xia, J. J. Yang, *Nat. Rev. Mater.* **2020**, *5*, 173.
[7] S. Menzel, M. Waters, A. Marchewka, U. Böttger, R. Dittmann, R. Waser, *Adv. Funct. Mater.* **2011**, *21*, 4487.
[8] K. Skaja, M. Andrä, V. Rana, R. Waser, R. Dittmann, C. Baeumer, *Sci. Rep.* **2018**, *8*, 10861.
[9] Y. Li, Z. Wang, R. M. Midya, Q. Xia, J. J. Yang, *J. Phys. D: Appl. Phys.* **2018**, *51*, 503002.
[10] P. R. Mickel, A. J. Lohn, B. J. Choi, J. J. Yang, M.-X. Zhang, M. J. Marinella, C. D. James, R. S. Williams, *Appl. Phys. Lett.* **2013**, *102*, 223502.
[11] M. T. Brumbach, P. R. Mickel, A. J. Lohn, A. J. Mirabal, M. A. Kalan, J. E. Stevens, M. J. Marinella, *J. Vac. Sci. Technol., A* **2014**, *32*, 051403.
[12] M.-J. Lee, C. B. Lee, D. Lee, S. R. Lee, M. Chang, J. H. Hur, Y.-B. Kim, C.-J. Kim, D. H. Seo, S. Seo, *Nat. Mater.* **2011**, *10*, 625.
[13] A. C. Torrezan, J. P. Strachan, G. Medeiros-Ribeiro, R. S. Williams, *Nanotechnology* **2011**, *22*, 485203.
[14] X. Lian, M. Wang, M. Rao, P. Yan, J. J. Yang, F. Miao, *Appl. Phys. Lett.* **2017**, *110*, 173504.
[15] Y. Guo, J. Robertson, *Appl. Phys. Lett.* **2014**, *105*, 223516.
[16] T. Heisig, K. Lange, A. Gutsche, K. T. Goß, S. Hambsch, A. Locatelli, T. O. Menteş, F. Genuzio, S. Menzel, R. Dittmann, *Adv. Electron. Mater.* **2022**, *8*, 2100936.
[17] A. Tsurumaki-Fukuchi, R. Nakagawa, M. Arita, Y. Takahashi, *ACS Appl. Mater. Interfaces* **2018**, *10*, 5609.
[18] L. Zhu, J. Zhou, Z. Guo, Z. Sun, *J. Phys. Chem. C* **2016**, *120*, 2456.
[19] S. Prada, M. Rosa, L. Giordano, C. Di Valentin, G. Pacchioni, *Phys. Rev. B* **2011**, *83*, 245314.

© 2022 The Authors. Advanced Electronic Materials published by Wiley-VCH GmbH

2199160x, 2023, 1, Downloaded from https://onlinelibrary.wiley.com/doi/10.1002/aelm.202200828, Wiley Online Library on [26/07/2023]. See the Terms and Conditions (https://onlinelibrary.wiley.com/terms-and-conditions) on Wiley Online Library for rules of use; OA articles are governed by the applicable Creative Commons License

[20] Y. Dai, Z. Pan, F. Wang, X. Li, *AIP Adv.* **2016**, *6*, 085209.
[21] H. Yildirim, R. Pachter, *ACS Appl. Mater. Interfaces* **2018**, *10*, 9802.
[22] H. Jiang, D. A. Stewart, *ACS Appl. Mater. Interfaces* **2017**, *9*, 16296.
[23] H. Yildirim, R. Pachter, *ACS Appl. Electron. Mater.* **2019**, *1*, 467.
[24] R. J. Bondi, M. P. Desjarlais, A. P. Thompson, G. L. Brennecka, M. J. Marinella, *J. Appl. Phys.* **2013**, *114*, 203701.
[25] R. J. Bondi, B. P. Fox, M. J. Marinella, *J. Appl. Phys.* **2016**, *119*, 124101.
[26] R. J. Bondi, M. J. Marinella, *J. Appl. Phys.* **2015**, *117*, 085308.
[27] R. J. Bondi, B. P. Fox, M. J. Marinella, *J. Appl. Phys.* **2017**, *121*, 214102.
[28] C. S. Pedersen, J. H. Chang, Y. Li, N. Pryds, J. M. G. Lastra, *APL Mater.* **2020**, *8*, 071108.
[29] L. Gao, Q. Ren, J. Sun, S.-T. Han, Y. Zhou, *J. Mater. Chem. C* **2021**, *9*, 16859.
[30] S. H. Lee, J. Moon, Y. Jeong, J. Lee, X. Li, H. Wu, W. D. Lu, A. Quantitative, *ACS Appl. Electron. Mater.* **2020**, *2*, 701.
[31] A. Siemon, S. Menzel, A. Marchewka, Y. Nishi, R. Waser, E. Linn, in *2014 IEEE Int. Symp. on Circuits and Systems (ISCAS)*, IEEE, Piscataway, NJ **2014**, pp. 1420–1423.
[32] M. Vos, P. L. Grande, S. K. Nandi, D. K. Venkatachalam, R. G. Elliman, *J. Appl. Phys.* **2013**, *114*, 073508.
[33] G.-S. Park, Y. B. Kim, S. Y. Park, X. S. Li, S. Heo, M.-J. Lee, M. Chang, J. H. Kwon, M. Kim, U.-I. Chung, R. Dittmann, R. Waser, K. Kim, *Nat. Commun.* **2013**, *4*, 2382.
[34] J. E. Stevens, A. J. Lohn, S. A. Decker, B. L. Doyle, P. R. Mickel, M. J. Marinella, *J. Vac. Sci. Technol., A* **2014**, *32*, 021501.
[35] G. C. Solomon, C. Herrmann, T. Hansen, V. Mujica, M. A. Ratner, *Nat. Chem.* **2010**, *2*, 223.
[36] S. Smidstrup, T. Markussen, P. Vancraeyveld, J. Wellendorff, J. Schneider, T. Gunst, B. Verstichel, D. Stradi, P. A. Khomyakov, U. G. Vej-Hansen, *J. Phys.: Condens. Matter* **2019**, *32*, 015901.
[37] R. Bartynski, D. Heskett, K. Garrison, G. Watson, D. Zehner, W. Mei, S. Tong, X. Pan, *Phys. Rev. B* **1989**, *40*, 5340.
[38] M. Marlo, V. Milman, *Phys. Rev. B: Condens. Matter Mater. Phys.* **2000**, *62*, 2899.
[39] A. Calzolari, A. Catellani, *IEEE Access* **2020**, *8*, 156308.
[40] D. A. Stewart, *Phys. Rev. Mater.* **2019**, *3*, 055605.
[41] V.-Q. Zhuo, Y. Jiang, M. Li, E. Chua, Z. Zhang, J. Pan, R. Zhao, L. Shi, T. Chong, J. Robertson, *Appl. Phys. Lett.* **2013**, *102*, 062106.
[42] J. M. Andrade, C. M. Rosário, S. Menzel, R. Waser, N. A. Sobolev, *Phys. Rev. Appl.* **2022**, *17*, 034062.
[43] G. Kresse, J. Furthmüller, *Comput. Mater. Sci.* **1996**, *6*, 15.
[44] G. Kresse, D. Joubert, *Phys. Rev. B* **1999**, *59*, 1758.
[45] J. P. Perdew, K. Burke, M. Ernzerhof, *Phys. Rev. Lett.* **1996**, *77*, 3865.
[46] J. Heyd, G. E. Scuseria, M. Ernzerhof, *J. Chem. Phys.* **2003**, *118*, 8207.
[47] A. V. Krukau, O. A. Vydrov, A. F. Izmaylov, G. E. Scuseria, *J. Chem. Phys.* **2006**, *125*, 224106.
[48] M. Magnuson, G. Greczynski, F. Eriksson, L. Hultman, H. Högberg, *Appl. Surf. Sci.* **2019**, *470*, 607.
[49] R. Ramprasad, *J. Appl. Phys.* **2003**, *94*, 5609.
[50] M. Gajdoš, K. Hummer, G. Kresse, J. Furthmüller, F. Bechstedt, *Phys. Rev. B* **2006**, *73*, 045112.
[51] H. Kramers, *Nature* **1926**, *117*, 774.
[52] R. L. de Kronig, *J. Opt. Soc. Am.* **1926**, *12*, 547.
[53] J. Harl, G. Kresse, L. D. Sun, M. Hohage, P. Zeppenfeld, *Phys. Rev. B: Condens. Matter Mater. Phys.* **2007**, *76*, 035436.
[54] L. Hedin, *Phys. Rev.* **1965**, *139*, A796.
[55] M. S. Hybertsen, S. G. Louie, *Phys Rev B Condens Matter* **1986**, *34*, 5390.
[56] R. Landauer, *IBM J. Res. Dev.* **1957**, *1*, 223.
[57] M. Brandbyge, J.-L. Mozos, P. Ordejon, J. Taylor, K. Stokbro, *Phys. Rev. B: Condens. Matter Mater. Phys.* **2002**, *65*, 165401.
[58] Atomistix ToolKit version 14.2, QuantumWise A/S, https://www.quantumwise.com (accessed: May 2022).
[59] M. Fuchs, M. Scheffler, *Comput. Phys. Commun.* **1999**, *119*, 67.
[60] H. Gao, A. Otero-de-la-Roza, S. Aouadi, E. Johnson, A. Martini, *Modell. Simul. Mater. Sci. Eng.* **2013**, *21*, 055002.

© 2022 The Authors. Advanced Electronic Materials published by Wiley-VCH GmbH

2199160x, 2023, 1, Downloaded from https://onlinelibrary.wiley.com/doi/10.1002/aelm.202200828, Wiley Online Library on [26/07/2023]. See the Terms and Conditions (https://onlinelibrary.wiley.com/terms-and-conditions) on Wiley Online Library for rules of use; OA articles are governed by the applicable Creative Commons License